Fluorinated Zn^{II} Porphyrins for Dye-Sensitized Aqueous Photoelectrosynthetic Cells

Alessio Orbelli Biroli,[a] Francesca Tessore,[b]* Gabriele Di Carlo,[b] Maddalena Pizzotti,[b] Elisabetta Benazzi,[c]* Francesca Gentile,[c] Serena Berardi,[c] Carlo Alberto Bignozzi,[c] Roberto Argazzi,[d] Mirco Natali,[c] Andrea Sartorel[e] and Stefano Caramori[c]

[a]Institute of Molecular Science and Technologies of the National Research Council (CNR-ISTM), SmartMatLab Centre, via Golgi 19, 20133 Milano, Italy

[b] Department of Chemistry, University of Milano, INSTM RU, via Golgi 19, 20133 Milano, Italy

[c]Department of Chemical and Pharmaceutical Sciences, University of Ferrara, Via L.Borsari 46, 44121, Ferrara

[d]CNR/ISOF c/o Department of Chemical and Pharmaceutical Sciences, University of Ferrara, Via L.Borsari 46, 44121, Ferrara

[e]Department of Chemical Sciences, University of Padova, Via Marzolo 1, 35131, Padova

corresponding authors:
francesca.tessore@unimi.it
Elisabetta:Benazzi@newcastle.ac.uk

Abstract

Three perfluorinated Zn^{II} porphyrins were evaluated as n-type sensitizers in photoelectrosynthetic cells for HBr and water splitting. All the dyes are featured by the presence of pentafluorophenyl electron withdrawing groups to increase the ground state oxidation potential and differ for the nature and the position of the π–conjugate linker between the core and the anchoring group tasked to bind the metal oxide, in order to assess the best way of coupling with the semiconductor. A phenyl-triazole moiety was used to link the carboxylic anchoring group onto *meso* position, while an ethynyl-phenyl linker was chosen to bridge carboxylic and cyanoacrylic groups onto β-pyrrolic position. A combination of electrochemical, computational and spectroscopic investigations confirmed the strong electron withdrawing effect of the perfluorinated porphyrin core which assures all the investigated dyes of the high oxidation potential required to the coupling with water oxidation catalysts (WOC). Such an electron-poor core, however, affects the charge separation character of the dyes, as demonstrated by the spatial distribution of the excited states, leading to a non-quantitative charge injection, although tilting of the molecules on the semiconductor surface could bring the porphyrin ring closer to the semiconductor, offering additional charge-transfer pathways.

Indeed all the dyes demonstrated successful in the splitting of both aqueous HBr and water, with the best results found for the SnO_2/TiO_2 photoanode sensitized with the β-substituted porphyrin equipped with a cyanoacrylic terminal group, achieving 0.4 and 0.1 mA/cm^2 photoanodic currents in HBr and water, respectively, under visible light. The faradaic yield for oxygen evolution in the presence of an Ir^{IV} catalyst was over 95% and the photoanode operation stable for more than 1000 seconds.

Thus the perfluorinated porphyrins with a cyanoacrylic anchoring group at the β-position should be considered for further development to improve the charge-transfer character.

Introduction

The implementation of a solar grid depends on strategies of energy storage, among which generation of solar fuels, where energy is stored in the form of chemical bonds of energy-rich molecules, is one of the most promising.[1,2] Besides splitting of water into hydrogen and oxygen, hydrohalic acid (HX) splitting and notably HBr splitting[3] by photoelectrochemical means (Dye-Sensitized Phtoelectrosynthetic Cells, DSPEC) is attracting an increasing interest by the scientific community. DSPECs based on polypyridine Ru^{II} complexes characterized by MLCT absorption centred at ca. 450 nm, have been reported to intercept the Br_2/Br^- couple with high efficiencies,

resulting in photocurrents in the mA range associated to the net production of H_2 and Br_3^- at the respective cathodic and photoanodic compartment of the cell.[4,5]

Among light-harvesting molecules for DSPEC, porphyrins are particularly promising, since they present various optical transitions in the visible region with high extinction coefficient (Soret or B band) covering the high energy portion of the visible spectrum and less intense, but broader, Q bands extending to the red. The electrochemical properties of Zn^{II} porphyrins can be easily tuned by varying the peripheral substituents,[6] resulting in some of the best performing dyes for dye sensitized regenerative solar cells.[7-9]

A symmetrical fluorinated porphyrin has been employed by Brudvig *et al.*[10] in conjunction with an iridium catalyst in a DSPEC for water splitting. This example was later followed by other works employing a perfluorinated *free-base* porphyrin based on hydroxamic acid linkage[11] and by other studies demonstrating the possibility of electron injection into semiconductors by porphyrins having very positive ground state potentials,[12,13,14,15] potentially useful for artificial photosynthesis.

In this contribution we focus on the electronic and photoelectrochemical properties of a series of Zn^{II} porphyrins (Figure 1), explored in the framework of photoelectrochemical cells for HBr and water splitting. With our molecular design we have tried to optimize charge separation at the semiconductor/dye interface by: 1) introducing four electron-withdrawing C_6F_5 groups in order to obtain an electron deficient tetrapyrrolic ring and increase the driving force for electron transfer in oxidation reactions involving the photooxidized dye, and 2) inserting a π-conjugated electron acceptor linker, equipped with either a carboxylic or a cyanoacrylic group, tasked to bind metal oxides and obtain the proper directionality of the excited state for charge injection. In addition, either β or *meso* substitution positions were explored in order to evaluate their impact on the dye energetics and sensitization efficiency.
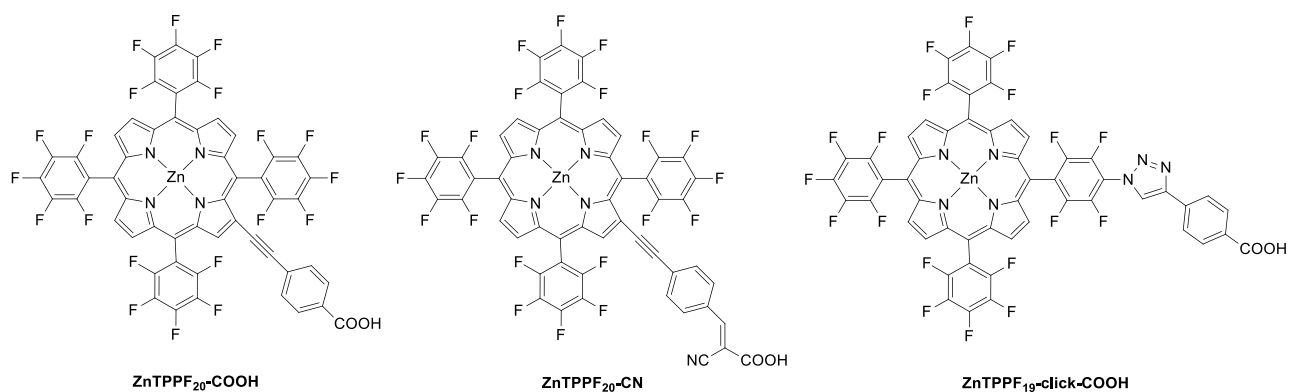

Figure 1. Zn^{II} porhyrins investigated in this work

Results and discussion

Syntheses

The syntheses of chromophores $ZnTPPF_{20}$-COOH and $ZnTPPF_{20}$-CN were performed according to Scheme 1.

The H_2TPPF_{20} porphyrin core was prepared in good yield by the Lindsey method,[16] through a $BF_3 \cdot OEt_2$ catalysed condensation of pyrrole with pentafluorbenzaldehyde, followed by oxidation of the porphyrinogen to porphyrin upon addition of DDQ.

The reaction of the *free-base* with $Zn(CH_3CO_2)_2 \cdot 2H_2O$ afforded the Zn^{II} complex in almost quantitative yield.

Then $ZnTPPF_{20}$ was monobrominated in β-pyrrolic position by reaction with *N*-bromosuccinimide (NBS), and the crude $ZnTPPF_{20}$-Br was immediately used for the following Sonogashira's coupling with 4-ethynylbenzoic acid or 4-ethynylbenzaldehyde to afford $ZnTPPF_{20}$-COOH or $ZnTPPF_{20}$-CHO respectively, with *N,N*-dimethylformamide as a solvent, triethylamine as a base and catalytic amounts of $[Pd(PPh_3)_4]$ and CuI, using a microwave assisted approach successfully developed by some of us to obtain β-substituted Zn^{II} porphyrins in good yield (1 hour reaction at 120 °C).[17]

Finally, a Knoevenagel condensation between $ZnTPPF_{20}$-CHO and cyanoacetic acid in $CHCl_3$ with piperidine as a base afforded $ZnTPPF_{20}$-CN in 56% yield.
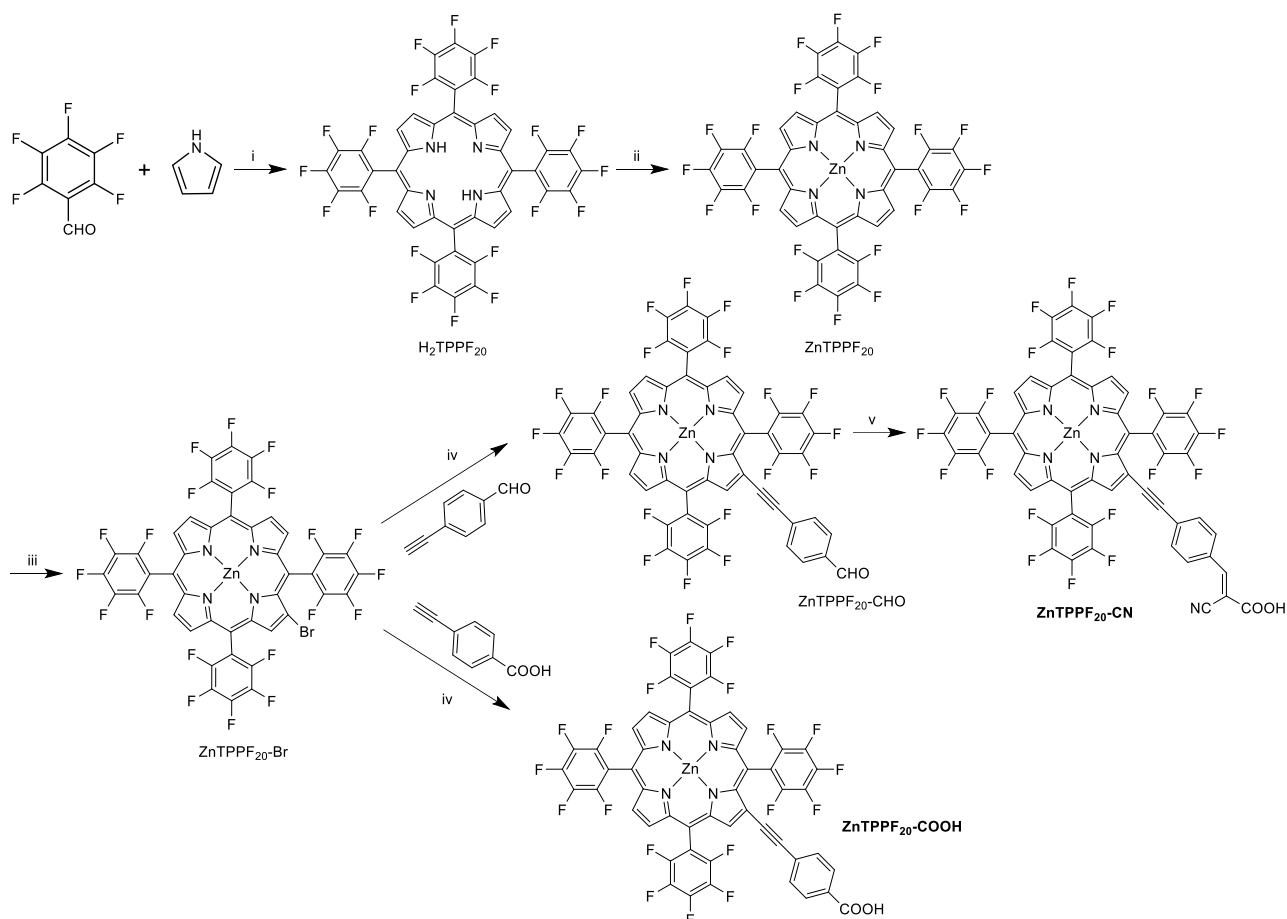
i) a) BF$_3$•OEt$_2$, N$_2$, CH$_2$Cl$_2$, RT, overnight; b) DDQ, CH$_2$Cl$_2$, RT, 2hrs, 61%. ii) Zn(CH$_3$CO$_2$)$_2$•2H$_2$O, CHCl$_3$, CH$_3$OH, reflux, 4hrs, >98%. iii) NBS, CH$_2$Cl$_2$, py, reflux, overnight, product not isolated. iv) NEt$_3$, [Pd(PPh$_3$)$_4$], CuI, DMF, MW 120°C, 1hr, 27% for ZnTPPF$_{20}$-COOH, 46% for ZnTPPF$_{20}$-CHO. v) CNCH$_2$COOH, CHCl$_3$, piperidine, reflux, overnight, 56.5%.

Scheme 1. Synthesis of β-pyrrolic substituted Zn^{II} porphyrins

The synthesis of ZnTPPF$_{19}$-click-COOH (Scheme 2) involved a "click-chemistry" approach. The selective nucleophilic substitution of only one of the four *para* fluorine atoms of the pentafluorophenyl rings in 5,10,15,20 *meso* position of H$_2$-PPF$_{20}$ was achieved by reaction of the *free-base* with 1 equivalent of sodium azide,[18] followed by complexation with Zn^{II}. Then, a Cu^{I} catalysed Huisgen 1,3-dipolar cycloaddition between ZnTPPF$_{19}$-N$_3$ and 4-ethynlbenzoic acid in a 1:1 THF/CH$_3$CN mixture,[19] with *N,N*-Diisopropylethylamine (DIPEA) as a base afforded ZnTPPF$_{19}$-click-COOH in 89% yield.
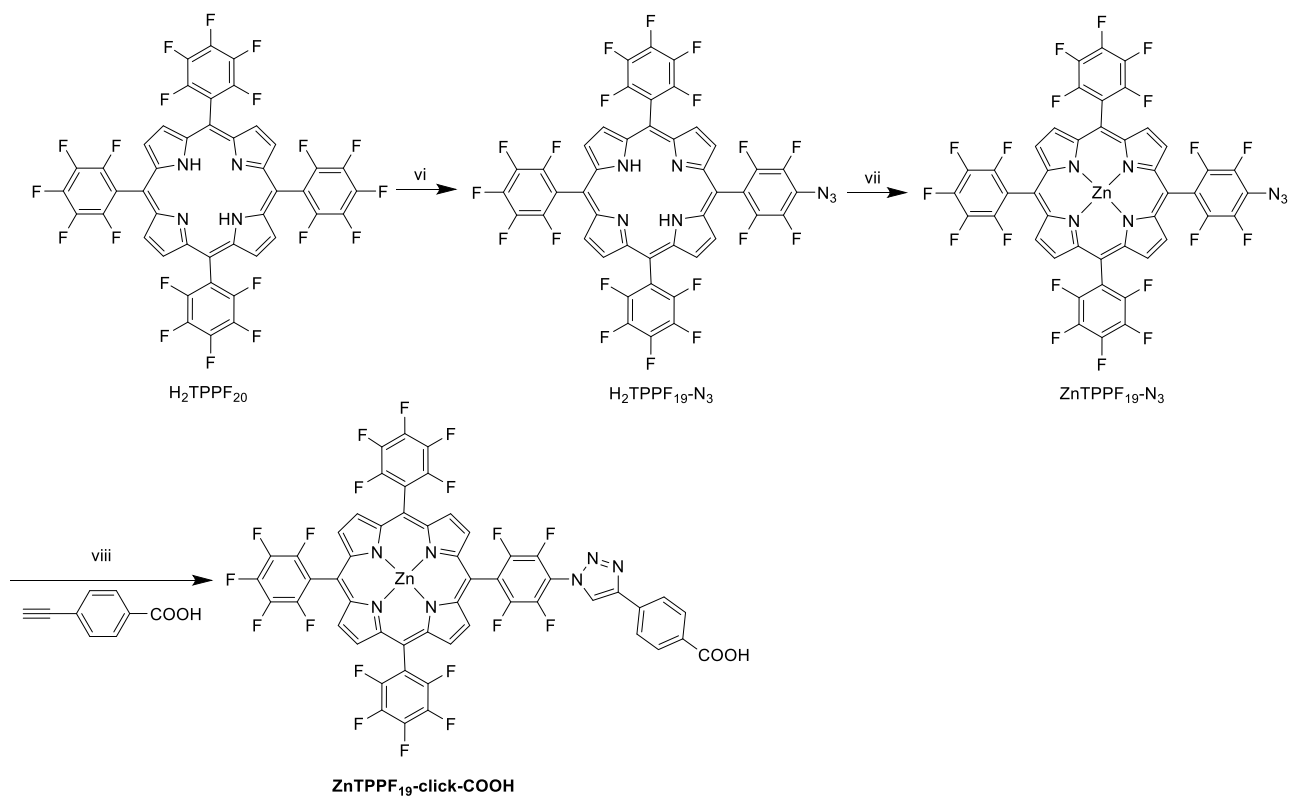
vi) NaN₃, N₂, DMF, 60°C, 3hrs, 47%. vii) Zn(CH₃CO₂)₂·2H₂O, CHCl₃, py, reflux, 4hrs, >98% . viii) DIPEA, CuI, N₂, THF/CH₃CN 1:1, RT, overnight, 89%.

Scheme 2. Synthesis of *meso*−substituted Zn^{II} click porphyrin

The three new dyes were characterized by ^{1}H- and ^{19}F-NMR spectroscopy (Figures S1-S3 in SI), elemental analysis and mass spectrometry (SI).

Spectroscopic and electrochemical properties in solution

All the dyes have been investigated by UV-vis spectroscopy in toluene solution and the ε-normalized spectra are reported in Figure 2.
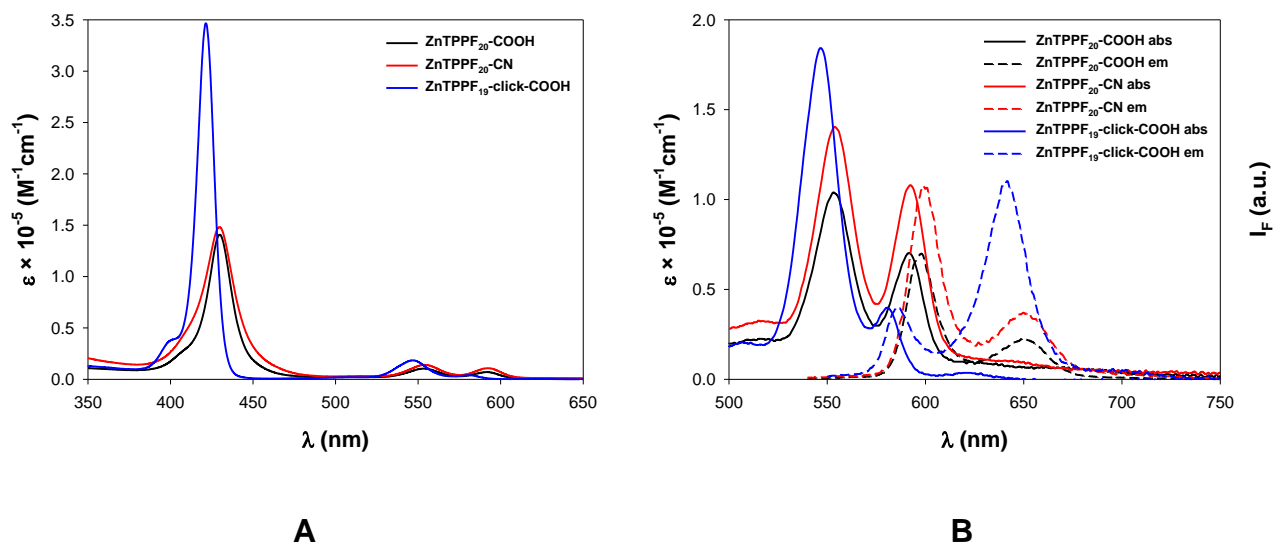
Figure 2. A) UV-vis spectra recorded in toluene solution; B) ε-normalized spectra of Q bands and emission spectra recorded in toluene solution at 10^{-6} M concentration

The spectra of ZnTPPF$_{20}$-COOH and ZnTPPF$_{20}$-CN (Figures 2A, S4 and S7 in SI) show the typical pattern of β-substituted Zn^{II} porphyrins with two evident Q bands and a sizeable red-shift of about 10 nm (for both B and Q bands) compared to the *meso*-substituted compound Zn-TPPF$_{19}$-click-COOH, indicating a more pronounced push-pull character for the β-substituted compounds. At the same time, the presence of the stronger acceptor cyanoacrylic acid group in ZnTPPF$_{20}$-CN barely affects the push-pull character as observed in other porphyrinic systems.[17,20] Therefore, the high degree of fluorination, which produces a strong electron-poor porphyrin core, is not weakening the effect of the cyanoacrylic group.

On the contrary, the absorption pattern of ZnTTPF$_{19}$-click-COOH (Figure S10) resembles that of *meso*-substituted porphyrins, where only one peak is clearly detectable for the Q band. However, a more detailed analysis reveals a second Q band at 581 nm featured by a very low intensity (Figure 2A).

Normalized emission spectra recorded for each dye at 10^{-6} M concentration in toluene solution are reported in Figure 2B and the relative data are summarized in Table 1.

As observed in the UV-vis spectra, β- and *meso*-substituted porphyrins present similar emission spectra reflecting the shape of their absorption Q bands. The excitation spectra (Figures S5, S8 and S11 in SI) superimpose with the relative UV-vis absorption spectra, indicating that population of the lowest emitting state occurs upon both the Soret and the Q bands excitation. Moreover, the minimal Stokes shift between the peak of the absorption band at lower energy and the peak of the emission band at higher energy, confirms the rigidity of these systems and reduced molecular structure distortions during the absorption and emission processes.

The lifetime has been measured in solution by the single photon counting using a pulsed laser source at 450 nm (see Experimental in SI), and from the deconvolution fitting of the decay profiles (Figures S6, S9 and S12 in SI), τ values in the range 1.3-1.6 ns for each dye have been recorded (Table 1). Quantum yield (QY, ϕ) of fluorescence have been measured in toluene solution at 10^{-6} M concentration obtaining values in the range of 2–4% (Table 1).

Finally, from the spectroscopic data recorded in toluene the E^{0-0} value has been calculated, which corresponds to the spectroscopic HOMO-LUMO energy gap (Table 1).

Table 1. Absorption and emission data in toluene solution and spectroscopic HOMO-LUMO energy gap

	λ_{Soret}/nm (logε)	λ_Q/nm (logε)	λ_{ex}/nm	λ_{em}/nm	τ/ns	Φ/%	E^{0-0}/eV
ZnTPPF$_{20}$-COOH	430 (5.15)	553 (4.02) / 592 (3.85)	430	598 / 649	1.6	2.5	2.09
ZnTPPF$_{20}$-CN	430 (5.17)	554 (4.15) / 592 (4.03)	430	599 / 650	1.6	3.9	2.08
ZnTPPF$_{19}$-click-COOH	421 (5.54)	547 (4.27) / 581 (3.60)	421	585 / 642	1.3	2.0	2.21

The electronic properties of the dyes have been investigated by cyclic voltammetry (CV) and compared to those of ZnTPPF$_{20}$ under the same experimental conditions, as a benchmark. Complete CV patterns obtained at 0.2 V/s on a glassy carbon (GC) electrode in 0.1 M tetrabutylammonium perchlorate (TBAP) in DMF solution are reported in the SI (Figures S13, S15, S17 and S19) and in Figure 3, and their key features are summarized in Table S1 in the SI.
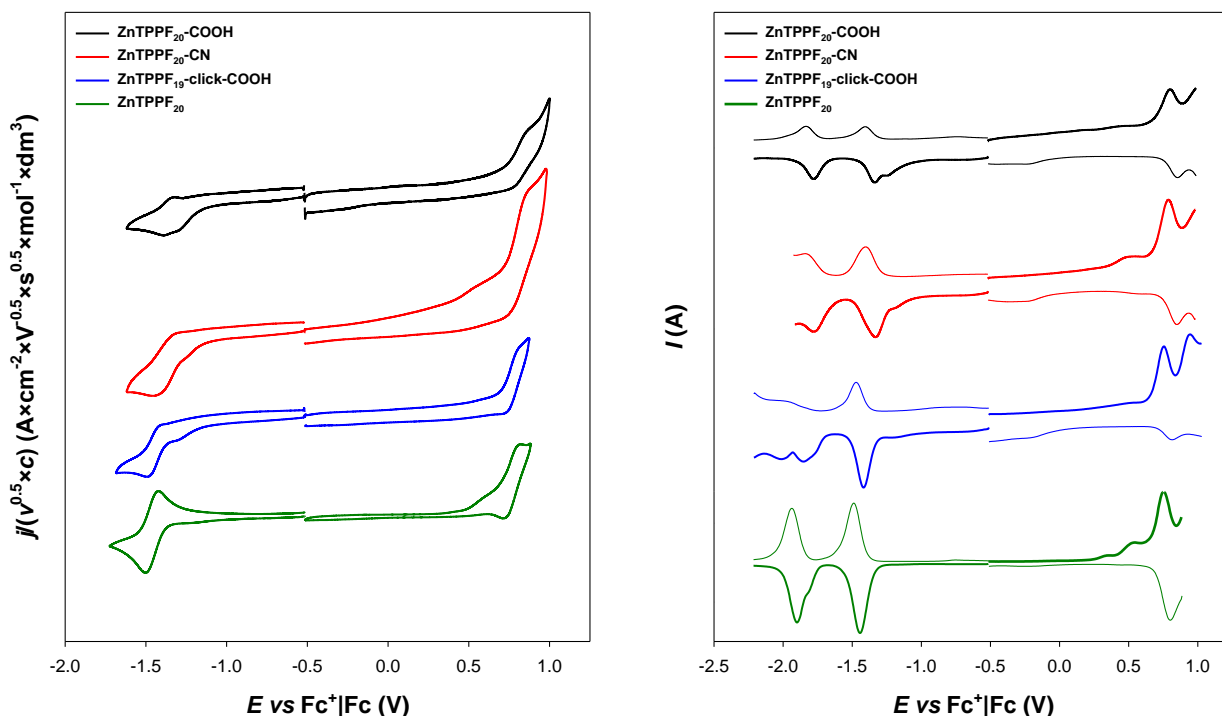

Figure 3. CVs including only first oxidation and reduction peaks (left) and DPVs including the second reduction process (right)

In all cases one oxidation peak and at least two reduction peaks have been observed in the potential window investigated, consistent with the electron-poor features of this class of perfluorinated porphyrins, resulting in a general anodic shift of the faradaic waves involving the frontier energy levels of these chromophores. The oxidation peak and the first reduction peak of each dye are reversible or quasi-reversible from both the electrochemical and chemical point of view, allowing for the calculation of the formal potentials of first oxidation (anodic, $E^{0'}_{pa}$) and first reduction (cathodic, $E^{0'}_{pc}$) processes in the chosen supporting electrolyte (formal potentials $E^{0'}$ approximate standard potentials E^0 under the assumption of neglecting the activity coefficients). The experimental $E^{0'}$ values also allow the evaluation of the electrochemical HOMO and LUMO energy levels,[6] and therefore of the HOMO–LUMO energy gap E_g (Table S1), employing the ferrocenium/ferrocene redox couple as a reference for intersolvental comparison of electrode potentials.[21]

The electrochemical HOMO-LUMO E_g of the β-substituted dyes are slightly higher than the spectroscopic ones (Table 1), in particular for ZnTPP$_{20}$-CN for which a narrower gap was expected. In search for a better resolution of the relevant electrochemical processes, DPV analysis has allowed a clearer determination of the peak potentials (Figure 3 and S14, S16, S18 and S20 in the SI). Moreover, a perfect correspondence with the CV data has been obtained for the dyes having a well-defined CV pattern, confirming the great potential of this technique for the evaluation of ambiguous cases.

The energy gaps obtained by DPV measurements (Table 2) are in good agreement with the spectroscopic data and with a narrower HOMO-LUMO gap achieved for the porphyrin endowed with a cyanoacrylic group, as reported in the literature.[17]

The *meso*-substitued ZnTPPF$_{19}$-click-COOH dye shows electrochemical potentials very similar to those of ZnTPPF$_{20}$, resulting in the same oxidation potential values, but in a slightly shifted reduction process. In general it can be concluded that the strongly oxidizing ground state potential of these species should allow to trigger energy demanding oxidation reactions, keeping at the same time sufficient driving force for the oxidative quenching of the excited state by charge injection to appropriate semiconductors.

Table 2. Key DPV features of dyes and benchmark, their electrochemical energy levels HOMO and LUMO derived therefrom $E^{0'}_{Ia}$ and $E^{0'}_{Ic}$ (or $E_{p,Ia}$ and $E_{p,Ic}$), all referred to $Fc^+|Fc$.
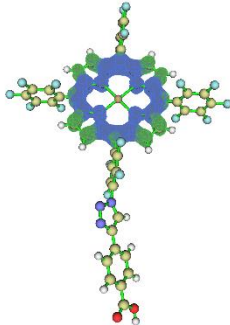
	$E_{p,Ia}/V$ $(Fc^+|Fc)$	$E^{0'}_{Ia}/V$ $(Fc^+|Fc)$	$E_{p,Ic}/V$ $(Fc^+|Fc)$	$E^{0'}_{Ic}/V$ $(Fc^+|Fc)$	HOMO/eV	LUMO/eV	$\Delta E^{0'}/V$ $(E_{g,EC}/eV)$
ZnTPPF$_{20}$-COOH	0.80	0.82	-1.34	-1.36	-5.62	-3.44	2.18
ZnTPPF$_{20}$-CN	0.79	0.81	-1.33	-1.35	-5.61	-3.45	2.16
ZnTPPF$_{19}$-click-COOH	0.75	0.77	-1.42	-1.44	-5.57	-3.36	2.21
ZnTPPF$_{20}$	0.75	0.77	-1.44	-1.46	-5.57	-3.34	2.23
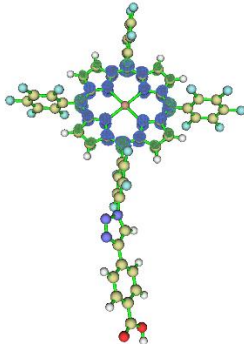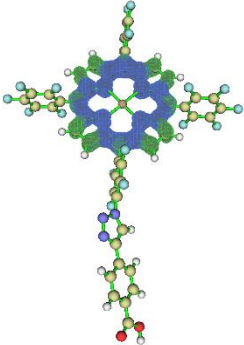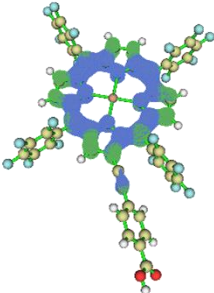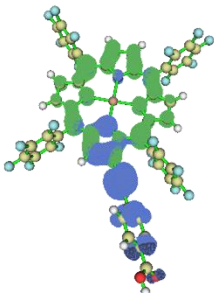
Computational Results

TDDFT calculations in THF (IEFCPM) at the B3LYP 6311 G* level[17] were used to extract information about the electronic distribution in the chromophores at their singlet ground and excited states. The EDDMs (Electron Density Difference Maps) generated from the Kohn-Sham (KS) orbitals ass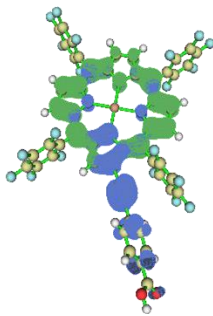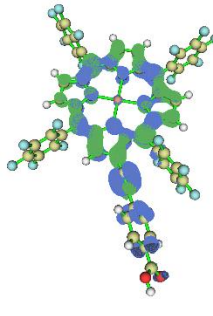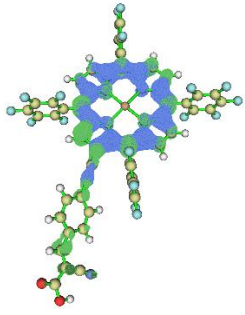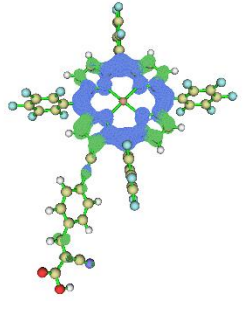ociated to the main electronic transitions in the visible region are shown in Table 3. The computed electronic transitions, the KS contributions to the calculated optical transitions and the KS orbitals involved in these latter are reported in Figures S21 and S22 in the SI and in Table 3. Generally, despite a systematic red shift (0.1-0.2 eV) of the most intense transition associated to the B band, the computation reproduces in an acceptable fashion the main spectral features of these fluorinated Zn^{II} porphyrins. In all cases the group of the most intense transitions falls in proximity of the experimental B band centred around 2.9 eV. Consistent with the experimental evidence, the *meso* ZnTPPF$_{19}$-click-COOH architecture is characterized by narrower B band, originated by two nearly degenerate transitions (2.3 and 3.06-3.07 eV, Table 3) from the highest occupied orbitals to LUMO and LUMO+1. In the case of ZnTPPF$_{20}$-CN and ZnTPPF$_{20}$-COOH a larger number of allowed transition occurs, broadening the B band, thanks to allowed excitations from HOMO-2 to LUMO +2. Indeed, while in ZnTPPF$_{19}$-click-COOH the B band excitation leads to ring centered EDDMs with practically no change in electronic density of the electron acceptor arm, the electronic redistribution following high energy optical excitation in ZnTPPF$_{20}$-CN and ZnTPPF$_{20}$-COOH shows a significant charge-transfer character, where, however, the linker arm is depleted of electronic density while the tetrapyrrolic ring is enriched, consistent with the strong electron withdrawing character induced by the perfluorinated substituents. Thus, in principle, in all cases, the electronic distribution upon interception of the B band is unfavorable to charge injection into the semiconductor. Concerning the lowest singlet state, generated upon Q bands excitation for energy $\geq$ 2.2 eV, weaker oscillator strengths are correctly predicted for all structures under examination. Again no involvement of the electron accepting arm is found for ZnTPPF$_{19}$-click-COOH (transition
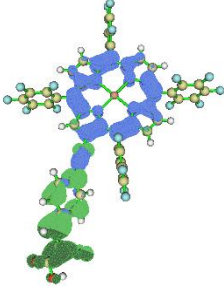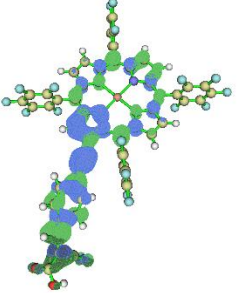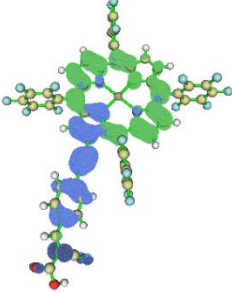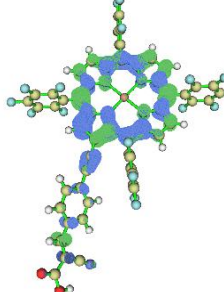
1 at 2.26 eV), while ZnTPPF$_{20}$-CN shows a small increase in the electronic density of the cyanoacrylic group, with most of the hole density delocalized on the ring. The largest electronic density on the arm is however found for transition 3 (2.58 eV). No involvement of the electron withdrawing arm is found with ZnTPPF$_{20}$-COOH either, probably due to the weaker electron accepting properties of its linker compared to that of ZnTPPF$_{20}$-CN. Higher energy excitations (> 2.23 eV) result in either π-π* states centered on the tetrapyrrolic structure or in their mixing with charge-transfer states shifting charge density from the linker to the electron-poor ring. Thus, calculations predict that in none of the chromophores under investigation a really satisfactory directionality of the excited states for electron injection is obtained, with the possible exception ZnTPPF$_{20}$-CN, for which some states, including the lowest one, could lead to an acceptable coupling for semiconductor sensitization. Clearly, the realistic situation on the disordered nanocystalline semiconductor is more complicated: tilting of the molecules on the semiconductor surface could bring the porphyrin ring closer to the semiconductor, in a situation favourable for through-space remote charge injection. The accidental proximity of the dye ring to other adjacent nanoparticles, may also offer additional charge-transfer pathways, which cannot be accounted for by this type of simple calculation.

Table 3. Hole (blue) and electron (green) density maps corresponding to optical transitions in perfluorinated Zn^{II} porphyrins. Transitions are numbered according to spectra S19

Transition number	Computed vertical excitation energies (eV/oscillator strength)	Experimentally observed band (eV) (band type)	Energy dispersion |ΔE| (eV) with respect to exp. band maximum	KS orbital contribution to excited state	Density map
ZnTPPF$_{19}$-click-COOH					
1	2.26/1.3 ×10^{-3}	2.25 (Q)	0.01	H-1 → L -0.17035 H-1 →L+1 0.46155 H → L 0.47475 H → L+1 0.17096	

2	3.06/1.876	2.96 (B)	0.09	H-8 → L -0.10630 H-1 → L 0.47859 H → L+1 0.48478	
3	3.07/1.522	2.96 (B)	0.10	H-8 → L+1 -0.11016 H-1 → L+1 0.48737 H → L -0.48419	
ZnTPPF$_{20}$-COOH					
2	2.26/0.044	2.22 (Q$_1$) 2.07 (Q2)	0.04 0.19	H-1 → L 0.19031 H-1 → L+1 0.41454 H → L 0.50371 H → L+1 -0.18224	
3	2.83/0.948	2.90 (B)	0.07	H-2 → L 0.53246 H-1 → L 0.14917 H-1 → L+1 0.28229 H → L -0.26882 H → L+1 0.17466	

4	3.00/0.8006	2.90 (B)	0.10	H-2 → L+1 0.40042 H-1 → L -0.34594 H-1 → L+1 0.20572 H → L -0.16015 H → L+1 -0.37446	
5	3.08/1.0446	2.90 (B)	0.18	H-3 → L 0.18509 H-2 → L 0.41892 H-1 → L+1 -0.36639 H → L 0.28678 H → L+1 -0.10032 H → L+2 0.14562	
ZnTPPF$_{20}$-CN					
1	2.22/0.203	2.22 (Q$_1$) 2.07 (Q2)	0.00 0.19	H-1 → L 0.21646 H-1 → L+1 -0.34679 H → L 0.52670 H → L+1 0.18437 H → L+2 -0.10319	
2	2.23/0.014	2.22 (Q$_1$) 2.07 (Q$_2$)	0.01 0.16	H-1 → L 0.47176 H-1 → L+1 0.17604 H-1 → L+2 -0.13478 H → L -0.22586 H → L+1 0.40923	

3	2.58/0.841	2.22 (Q1)	0.36	H-2 → L -0.18134 H-1 → L+1 0.32706 H → L 0.33183 H → L+1 0.110406 H → L+2 0.47185	
5	2.79/0.549	2.90 (B)	0.11	H-2 → L 0.56634 H-1 → L+1 -0.15159 H-1 → L+2 0.16548 H → L+2 0.33595	
6	3.01/0.400	2.90 (B)	0.11	H-2 → L+1 0.51314 H-1 → L 0.16443 H-1 → L+1 -0.11269 H-1 → L+2 -0.28653 H → L+1 -0.31030	
7	3.13/1.319	2.90 (B)	0.23	H-2→ L 0.17876 H-2 → L+1 0.28888 H-2 → L+2 -0.30189 H-1 → L+1 0.34701 H-1 → L+2 0.12718 H → L 0.16246 H → L+1 0.12075 H → L+2 -0.27810	

Spectroscopic and electrochemical characterization of the sensitized photoanodes

Adsorption from 0.1 mM dye solutions on TiO_2 leads to a very high absorption in the Soret band region, which in all cases saturated the instrumental response absorbance values greater than 3, while the absorbance in the Q region varies in the order $ZnTPPF_{20}$-CN (≈ 0.9) > $ZnTPPF_{20}$-COOH (≈ 0.7) > $ZnTPPF_{19}$-click-COOH (≈ 0.5) (Figure S23). Absorption spectra thus point to a better surface uptake of the β structures compared to *meso*-$ZnTPPF_{19}$-click-COOH having the highest molar extinction coefficients. At the same time the better harvesting achieved by $ZnTPPF_{20}$-CN is probably due to both its stronger dipole moment and superior affinity to the TiO_2 surface with respect to $ZnTPPF_{20}$-COOH. Sensitization of SnO_2 electrodes (Figure S24) results in the same trend already described with TiO_2, but the optical density of the resulting photoanodes was considerably lower, with maximum values in the B band of the order of ≈ 0.6. The dye uptake by SnO_2 thin films could be improved by treating them with $TiCl_4$ followed by firing at 450 °C in order to form a nanometric coating of TiO_2 on top of the SnO_2 nanoparticles and increase the surface area and the reactivity for dye adsorption. AFM maps of the SnO_2 electrodes following $TiCl_4$ treatment show an increased surface roughness (Figure S27), with R_q increasing from 30.9 µm to 47.1 after the treatment, without a noticeable increase the SnO_2 nanoparticle size, having a diameter varying from 20 to 40 nm (Figure S28 and S29). This evidence is consistent with the coverage of SnO_2 by thin TiO_2, which cannot be clearly resolved in our AFM maps on such type of disordered substrate but is evident in the form of a micro-roughenss in the cross sectional analysis by sampling along various directions of the imaged surface portion at high magnification. As a result, the absorbance of SnO_2/TiO_2 electrodes loaded with the series Zn^{II} porphyrins more than doubles relative to unmodified SnO_2, reaching a close-to-unity light harvesting in the Soret region (Figure 4A). By using $A(\lambda)=1000\varepsilon(\lambda)\Gamma$ it is possible to calculate the surface loading Γ of the dyes, of the order of 2×10^{-8} Mol/cm^2, in good agreement with ICP results based on Zn determination, affording values around 1.7×10^{-8} Mol/cm^2. The SnO_2/TiO_2 photoanodes were thus preferred over the SnO_2 ones for the subsequent photophysical and photoelectrochemical investigations. It is also interesting to evaluate the impact of the $TiCl_4$ treatment on the SnO_2 energetics, which can be conveniently studied by electrochemical means in a solvent medium relevant to the intended use of such photoanodes. In aqueous 0.1 M HBr + 0.4 M NaBr, SnO_2 is characterized by a broad reductive wave which appears chemically reversible (Figure S30), having onset at ca 0.3 V vs SCE, followed by a small hump centred at ca. 0.2 V, assigned to the filling of surface states as the potential is scanned towards negative values. A change in the J/E slope occurs at ca. -0.05 V vs SCE probably indicating the threshold of the reduction of conduction band states. Consistent with the n-type nature of SnO_2 in the chosen electrolyte, no faradaic processes are observed in the interval 0.3/0.6 V vs SCE where a small capacitive current (ca. 1µA) flows. SnO_2/TiO_2 electrodes (Figure S30)

maintain the same conduction band edge energetics as of those of bare SnO_2, with a clear reductive wave having onset between 0 and -0.05 V vs SCE, but the electrochemical processes originating from sub-band gap states are dramatically reduced in intensity, consistent with the passivation of many SnO_2 surface states by the TiO_2 layer. Adsorption of $ZnTPP_{20}$-CN does not change the surface energetics significantly, being the electrochemical features practically coincident with that of the undyed electrode in the -0.2/0.8 V vs SCE interval (Figure S32). A notable exception occurs at potentials higher than 1 V vs SCE, where the electrocatalytic oxidation of Br^- mediated by the surface adsorbed dye becomes evident, with an irreversible wave having a ×10 increased intensity compared to the same process observed at bare SnO_2/TiO_2 (in this latter case the oxidation process occurs ostensibly at some exposed FTO). This is already a qualitative confirmation of the ability of the oxidized porphyrins to intercept the redox chemistry of the Br^-/Br_3^- couple.

(A)   **(B)**
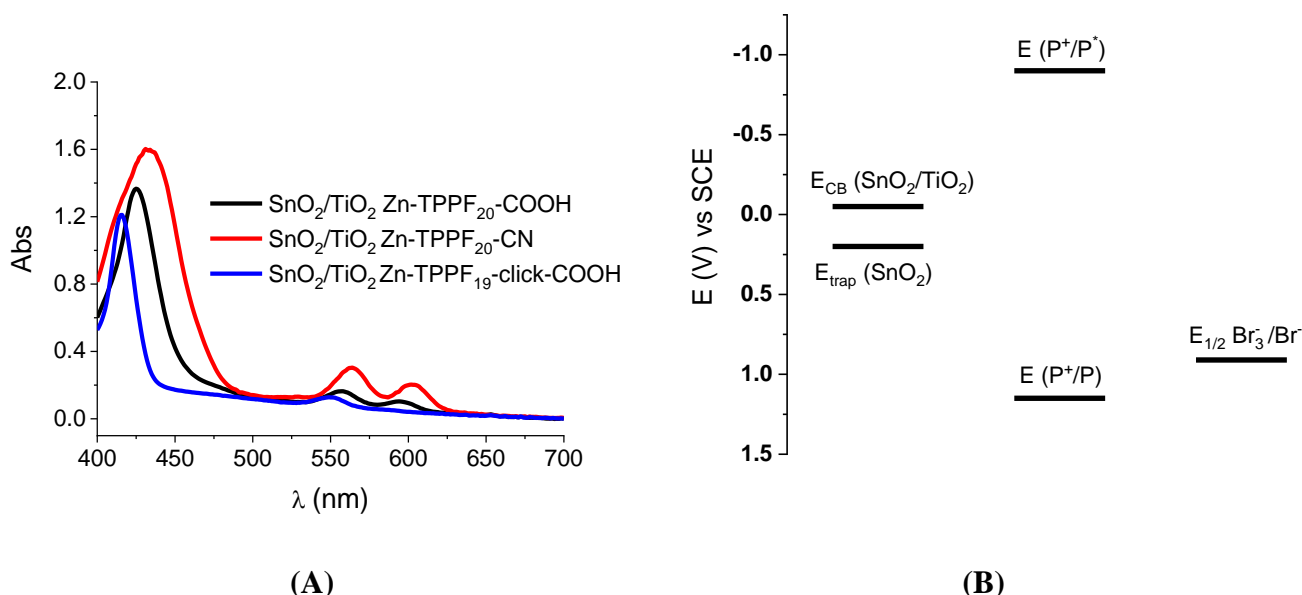
Figure 4. (A) Absorption spectra of SnO_2/TiO_2 electrodes sensitized with Zn-TPP_{20}-COOH, Zn-TPP_{20}-CN and Zn-TPP_{19}-click-COOH; **(B)** Electrochemical levels relevant to the photoelectrochemical process in 0.1 M HBr/0.4 M NaBr. The diagram was built by considering the onset of the reductive processes of the different semiconductor films together with the energy levels of $ZnTPPF_{20}$-CN from Table 4. The half wave potential of the Br_3^-/Br^- couples was measured by cyclic voltammetry at a glassy carbon electrode at pH 1. Notice that Zn-$TPPF_{20}$-CN was used to exemplify the energetics common to the porphyrin (P) series under consideration and that that the $E_{1/2}$ potential of the redox couple may not describe the details of the energetics involved in the photoinduced oxidation of Br^-.[2,4]

Finally, while data in Table 2 are useful to understand the general electronic properties of the dye series under investigation, the energetics relevant to charge injection and regeneration are more properly accounted for by including the interaction of the dye with the semiconductor oxide and the influence of operational solvent chosen for the DSPEC (water), wherein electrochemical measurements in solution are precluded due to solubility. Emission spectra and DPV were recorded on SnO_2 treated with $TiCl_4$: the emission spectra (Figure S25) show the vibronic components associated to the lowest excited singlet state, with a slight blue-shift with respect to the measurements in organic solution, from which the E^{0-0} spectroscopic energy can be determined. DPV afforded (Figure S26, Table 4) the first ground state oxidation potential (E_{pa}), and the first excited state oxidation potential was consequently calculated according to $E_{ox}^*=E_{pa}-E^{0-0}$. These three structures exhibit similar ground and excited state energetics, with first excited state oxidation potential sufficiently negative for injection into semiconductor electrodes and a sufficiently positive ground state to trigger, in principle, oxidation of bromide or activate water oxidation catalysts. The electrochemical potentials of interest to the sensitization processes, by considering SnO_2/TiO_2 electrodes, are summarized in Figure 4B, where $ZnTPPF_{20}$-CN was used to exemplify the energetics common to the porphyrin (P) series under consideration.

Table 4. Spectroscopic energy (E^{0-0}), anodic peak potential (E_{pa}) and oxidation potential (E_{ox}^*) of SnO_2/TiO_2 electrodes modified with $Zn-TPP_{20}$-COOH,/$Zn-TPP_{20}$-CN, $Zn-TPP_{19}$-click-COOH. Measurements performed on the thin films in contact with in 0.1 M $HClO_4$

	E^{0-0}	E_{pa} (V vs SCE)	E_{ox}^* (V vs SCE)
$ZnTPPF_{20}$-COOH	2.04	1.20	-0.84
$ZnTPPF_{20}$-CN	2.05	1.15	-0.9
$ZnTPPF_{19}$-click-COOH	2.09	1.17	-0.92

Transient Absorption Spectroscopy

Transient Absorption (TA) spectra, following 532 nm excitation of $ZnTPPF_{20}$-CN either in toluene solution or loaded on TiO_2 or SnO_2/TiO_2 thin films are reported in Figure 5. $ZnTPPF_{20}$-COOH and $ZnTPPF_{19}$-click-COOH share qualitatively common spectroscopic features with those of $ZnTPPF_{20}$-CN and are reported, for brevity, in the ESI (Figure S33, S35 and S36).
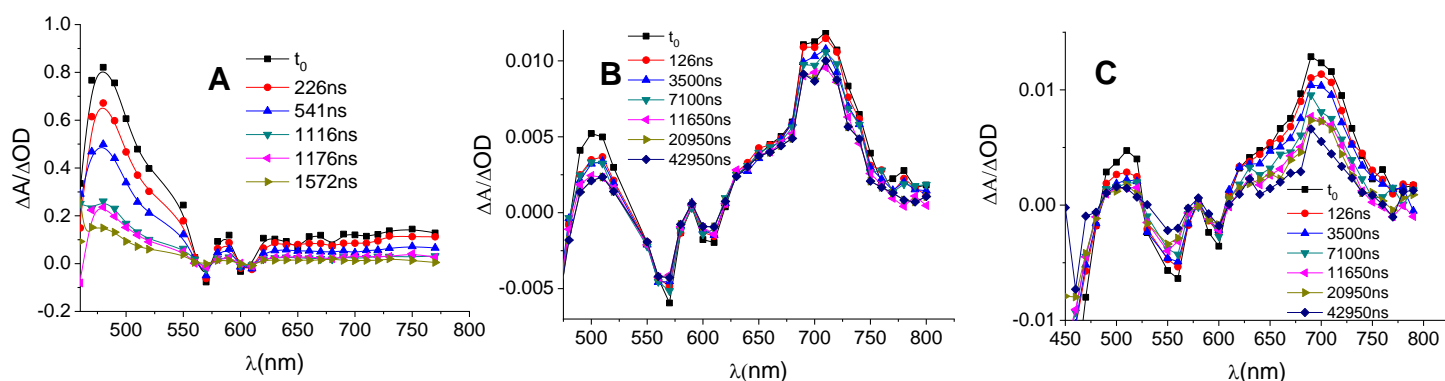
Figure 5. A) Transient absorption spectra of ZnTPPF$_{20}$-CN in toluene solution (5×10^{-4}M); B) loaded on TiO$_2$; C) loaded on SnO$_2$/TiO$_2$. Thin films were in contact with 0.1 M NaClO$_4$ at pH 3. Oscilloscope Input impedance 350 Ω.

The TA spectra of ZnTPPF$_{20}$-CN in 5×10^{-4}M toluene solution (Figure 5A), are consistent with the formation of the population of the T1 state, dominated by the strong absorption centered at 500 nm, whose formation falls within the pulse and disappears completely within about 10 microseconds (Figure 5A). The 500 nm absorption is followed by the ground state bleaching and by a flat and featureless absorption extending to the NIR. Such features have been observed in other β-substituted porphyrins carrying donor and acceptor groups,[22] but are also typical of more symmetric structures,[23] where the lowest electronic states are prevailingly localized on the tetrapyrrolinc ring, indicating a relatively small influence of the electron withdrawing linker arm on the electronic properties of the lowest excited state.

TA spectra of the dye-sensitized semiconductors are characterized, along with the Q band bleaching at 570 and 610 nm, by a well-defined sharp absorption band centered around 700 nm, which is assigned to the oxidized dye ZnTPPF$_{20}$-CN$^+$ formed upon charge injection into the semiconductor. On TiO$_2$ the spectral signature of the oxidized dyes is accompanied by the 500 nm absorption feature of the excited state decreasing by 33 % during the first 120 ns, whereas in other spectral regions where the excited state absorption is less important, a marginal evolution of TA spectra is found. For example, the 710 nm band, dominated by ZnTPPF$_{20}$-CN$^+$ is reduced, due to recombination, by just ca. 3% on a comparable time scale. The residual T1 absorption indicates that, at least for a fraction of the ZnTPPF$_{20}$-CN population adsorbed on TiO$_2$, the intersystem crossing process from S1 to T1 is kinetically competitive with charge injection into the semiconductor and that, ostensibly, T1 is not capable to inject.[24]

Ultrafast measurements on structurally related, albeit not identical, compounds, revealed that intersystem crossing on push-pull β porphyrins occurs within 200/400 ps, setting thus a lower limit

for the charge injection rate constant on similar time scales.[25] The triplet residue on TiO_2 film is even more pronounced in $ZnTPPF_{20}$-COOH and $ZnTPPF_{19}$-click-COOH (Figure S35), confirming, in qualitative agreement with the calculations, the better directionality and surface coupling of the lowest $ZnTPPF_{20}$-CN singlet state for charge injection.

The observation of excited state residual on TiO_2 is somewhat surprising, in consideration of the dye excited state oxidation potential of the order of -0.8/-0.9 V vs SCE, while the flat band potential of TiO_2 can be estimated (in V vs SCE) according to V_{fb}= -0.4 – 0.06 × pH.[26] The activation energy for the electron transfer, ΔG^*_{ET}, is given, according to the classical Marcus expression by (ΔG_{ET}^*= $(E^*_{ox}-E_{FB}+\lambda)^2/4\lambda)$[27] where the reorganization energy $\lambda = \lambda_{in} + \lambda_{out}$ of symmetrical porphyrins in apolar solvents, such as toluene, was estimated of the order of 0.4 eV.[28] However, it has been also reported that the presence of perfluorinated groups may increase significantly λ_{in} due to high-frequency C-F stretching associated to the contraction and expansion of the porphyrinic core, up to doubling the value reported in the presence of conventional C-H bonds (*i.e.* 0.8 eV).[29] It has also to be considered that the outer contribution λ_{out} increases in aqueous media, where reorganization of solvent dipoles is important. By taking into account these facts, the electron transfer from the excited dye to TiO_2 in aqueous acidic medium (from pH 1 to pH 3, which are the conditions explored in this work) may become activated in the presence of reorganization energy of the order of 0.8-1 eV, which appears to be a reasonable estimate in consideration of references 27 and 28 and our electrolyte conditions. In order to check whether thermodynamic, besides electronic, limitations to the charge injection kinetics are present, we explored the TA of the dyes loaded on SnO_2/TiO_2 electrodes, where we hoped that the thin TiO_2 layer, created on top of SnO_2 upon $TiCl_4$ hydrolysis was not constituting a significant barrier to electron transfer.

On SnO_2/TiO_2 (Figure 5C) the absorption intensity of the excited state residue associated to the T1 state is decreased compared to the 710 nm feature, ($\Delta A_{710}/\Delta A_{500}$ = 2.3 on TiO_2; $\Delta A_{710}/\Delta A_{500}$ = 2.8 on SnO_2/TiO_2) indicating, on SnO_2/TiO_2, a higher yield of charge injection, consistent with the larger driving force offered by the lower flat band potential of SnO_2 (ca. 0.2 V vs SCE) compared to TiO_2. Again, the same trend is observed for $ZnTPPF_{20}$-COOH and $ZnTPPF_{19}$-click-COOH (Figure S36). Finally we can observe that, once generated, the charge separated state (CS) is, long lived with either TiO_2 or SnO_2/TiO_2, its recovery far from being complete on a time scale of 50 μs, leaving in principle sufficient time for intercepting redox reactions of potential interest in the field of energy storage. In the following discussion the indications extracted by TAS are corroborated by photoelectrochemical measurements in the presence of hole scavengers.

Photoelectrochemical properties in the presence of hole scavengers

Photocurrents registered with the porphyrin-sensitized TiO_2 photoanodes under AM 1.5 G light (0.1 W/cm^2) in the presence of 0.1M HBr are reported in Figure S37. The photocurrent onset is observed between -0.1 V and -0.2 V vs SCE and rises by moving to positive potentials, as expected from an n-type/electrolyte junction. The limiting value is reached in all cases at ca. 0.2 V vs SCE, but the photocurrent is generally very modest. TiO_2/ZnTPPF$_{20}$-CN represents the best photoanode, yielding up to 40 μA/cm^2 net photocurrent at 0.2 V vs SCE, while TiO_2/ZnTPPF$_{20}$-COOH and TiO_2/ZnTPPF$_{19}$-click-COOH gave plateau values of 30 and 10 μA/cm^2, respectively. Despite the modest conversion, the photo-action spectra, regardless of the substrate on which they were recorded (Figure S42 and Figure 7), are sensibly consistent with the related absorption spectra of the thin films, confirming in all cases the involvement of the excited state of the porphyrin in the sensitization process. The use of SnO_2 films to oxidatively quench the excited state of dyes which are not capable of efficient injection into TiO_2 has been reported by Bergeron et al.,[30] and, similarly to Indium Tin Oxide (ITO)[31] has been later implemented in DSPECs by other authors, often in combination with ALD-deposited overlayers with the task of prolonging the lifetime of the charge separated state at the semiconductor/electrolyte interface.[32,33]

J/E characteristics recorded with 0.1 M HBr with SnO_2/TiO_2 sensitized photoanodes undergo a 5 to 10 fold increase in photocurrent, compared to TiO_2, consistent with an improved charge injection by the excited state of the Zn^{II} porphyrins and retarded recombination owing to surface state passivation by TiO_2. The J/E curves evidence a positive shift of the photoanodic threshold, in agreement with the expected flat band of SnO_2, ca. 0.2 V vs SCE. Photocurrent plateau values in 0.1 M HBr are generally found at ca. 0.35 V vs SCE and vary in the order ZnTPPF$_{20}$-CN ($\approx$ 0.35 mA/cm^2) > ZnTPPF$_{19}$-click-COOH ($\approx$ 0.2 mA/cm^2) > ZnTPPF$_{20}$-COOH ($\approx$ 0.15 mA/cm^2) (Figure S38). By contrast, the undyed electrode produces a marginal photocurrent (< 5 μA/cm^2) while, in the dark, the electrochemical oxidation of Br$^-$ occurs at ca. 0.8 V vs SCE, probably through pinholes in the film, leaving exposed FTO sites. Nevertheless the anodic current, out to 1 V vs SCE, is very small, ca. 2.5 μA/cm^2 (Figure S40). This means that at least 0.6 eV can be stored in the sensitized single junction, consistent with the expected difference between quasi Fermi level of the photoanode, apparently pinned on the SnO_2/TiO_2 surface states and the Fermi level of the electrolyte. Better passivation of the interface and quantitative dye regeneration by the electrolyte are expected to further improve cell energetics.

An optimized performance was found employing a mixture of 0.3 M NaBr and 0.1 M HBr (Figure 6), where ZnTPPF$_{20}$-CN generated a steady state limiting value of 0.4 mA/cm^2, with transients reaching 0.5 mA/cm^2, showing a good match with the shape of the current potential characteristics. Reproducibility in photoanode performance under [Br$^-$] = 0.4 M was good, as shown by statistical

error bars in a range of ca. 10 % with respect to the average photocurrent plateau value (Figure 6D). Further attempts by increasing the [Br⁻] up to 0.5 M and above were unfortunately unsuccessful, as the unstable operation of the cell was observed, associated to spectral changes the Q band structure which suggested porphyrin demetallation under such circumstances. Otherwise, in 0.4 M Br⁻ the dye stability was satisfactory and no decrease in the dye absorption nor modification of the spectral features of $ZnTPPF_{20}CN$ was observed, with Soret and Q bands maintaining their shape and relative intensity. Only a blue shift of a few nm was observed and tentatively ascribed to Stark perturbation upon surface adsorption of protons, following immersion and potentiodynamic cycling in the acidic electrolyte medium (Figure S39).
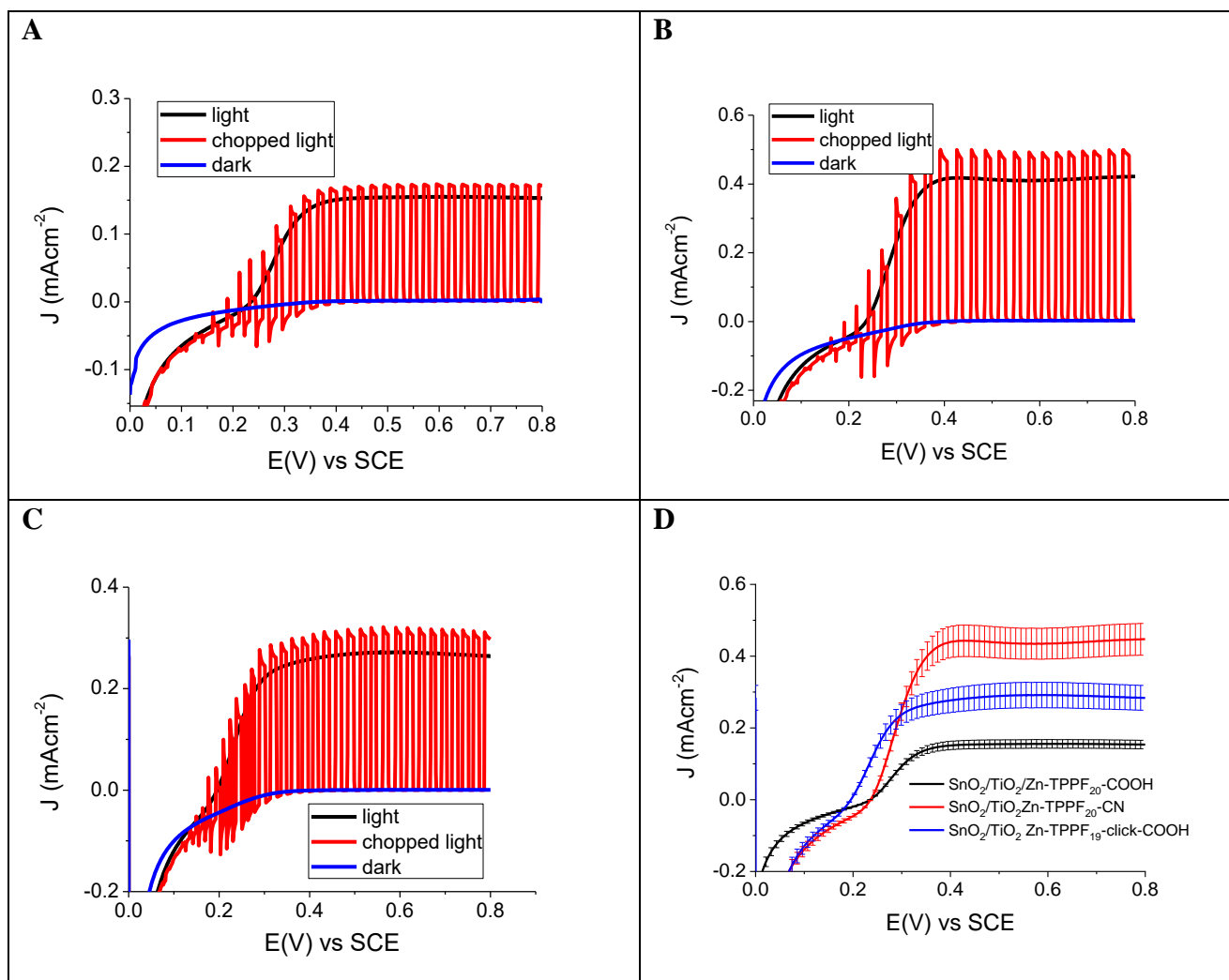

Figure 6. Current voltage curves recorded with SnO_2/TiO_2 photoanodes in HBr 0.1M, NaBr 0.3M under AM 1.5 G. a) $ZnTPP_{20}$-COOH, b) $ZnTPP_{20}$-CN, c) $ZnTPP_{19}$-click-COOH Photoanodes irradiated from the FTO side, d) Averaged J/V curves taken on a series of 10 photoanodes.

Even in our optimized electrolyte conditions, the photoaction spectra, whose conversion efficiencies agree with the trend outlined by the J/E curves, show modest charge separation efficiencies. Maximum conversions of the order of ca. 7 % and 2 % are observed with 0.4 M Br⁻ in

correspondence of the respective B and Q manifold of the best dye $ZnTPPF_{20}$-CN, which, given the homogeneous ground and excited state properties found within the series under investigation, probably benefits most of the better electronic coupling offered by the cyanoacrylic group. The corresponding APCE spectra (Figure S43) are quite constant throughout the visible range, indicating that quantum yield of charge injection is substantially independent from the state which is initially populated by light absorption, a statement not necessarily true when ultrafast charge injection is in kinetic competition with thermalization of the electronic excited states. While injection can still be less than optimal with SnO_2/TiO_2 substrates, these low conversion values could also be indicative of kinetic competition between dye regeneration by Br^- and recombination, as already suggested by the strong impact of electrolyte composition on photoanode performance. Recombination kinetics involving $SnO_2/TiO_2/ZnTPPF_{20}$-CN fully develop in the millisecond time domain and were monitored at 700 nm in the presence of Br^- 0.4 M (pH 1) at 0. 7 V vs Pt, a voltage falling well within the limiting photocurrent of the photoanode, corresponding thus to the maximum bias-assisted charge separation rate (Figure S44 and Table S3). In the presence of HBr, a substantial shortening of the oxidized dye decay is observed (Figure 7D), due to electron donation by Br^-, affording a regeneration efficiency η_{reg} = 49% (Table S4). Let aside electronic effects, such value could not come as a surprise in consideration of the ground state oxidation potential (ca. 1.2 V vs SCE) of the porphyrin, less positive of ca. 0.4 V compared those of other dyes (ca. 1.6 V vs SCE), which exhibited nearly unitary η_{reg}.[4] From APCE = $\Phi_{inj}\eta_{reg}$, assuming negligible losses due to electron recapture by Br_3^-, we obtain a charge injection yield of the order of 14%. Such value is in good agreement with APCE spectra obtained in the presence of ascorbic acid (AA), a better hole scavenger than Br^-, generating, in the best case represented again by Zn-$TPPF_{20}$-CN, photocurrents of 1.5 mA/cm^2 at 0.7 V vs SCE (Figure S41) and APCE of the order of 16-18 % (Figure S43C). Actually, in the presence of ascorbic acid, TA spectra revealed the formation of the radical anion of the porphyrin (Figure S34), living hundreds of μs in deareated DMSO, indicating that injection might also occur from the long lived reduced state of the porphyrin, as a result of the triplet reductive quenching by ascorbic acid. Injection from reduced state was observed previously in the case of other poorly reducing Ru^{II} sensitizers.[34] This would also explain the slightly higher injection yield calculated with AA with respect to the approximate estimate obtained at the same pH in the presence of Br^-.
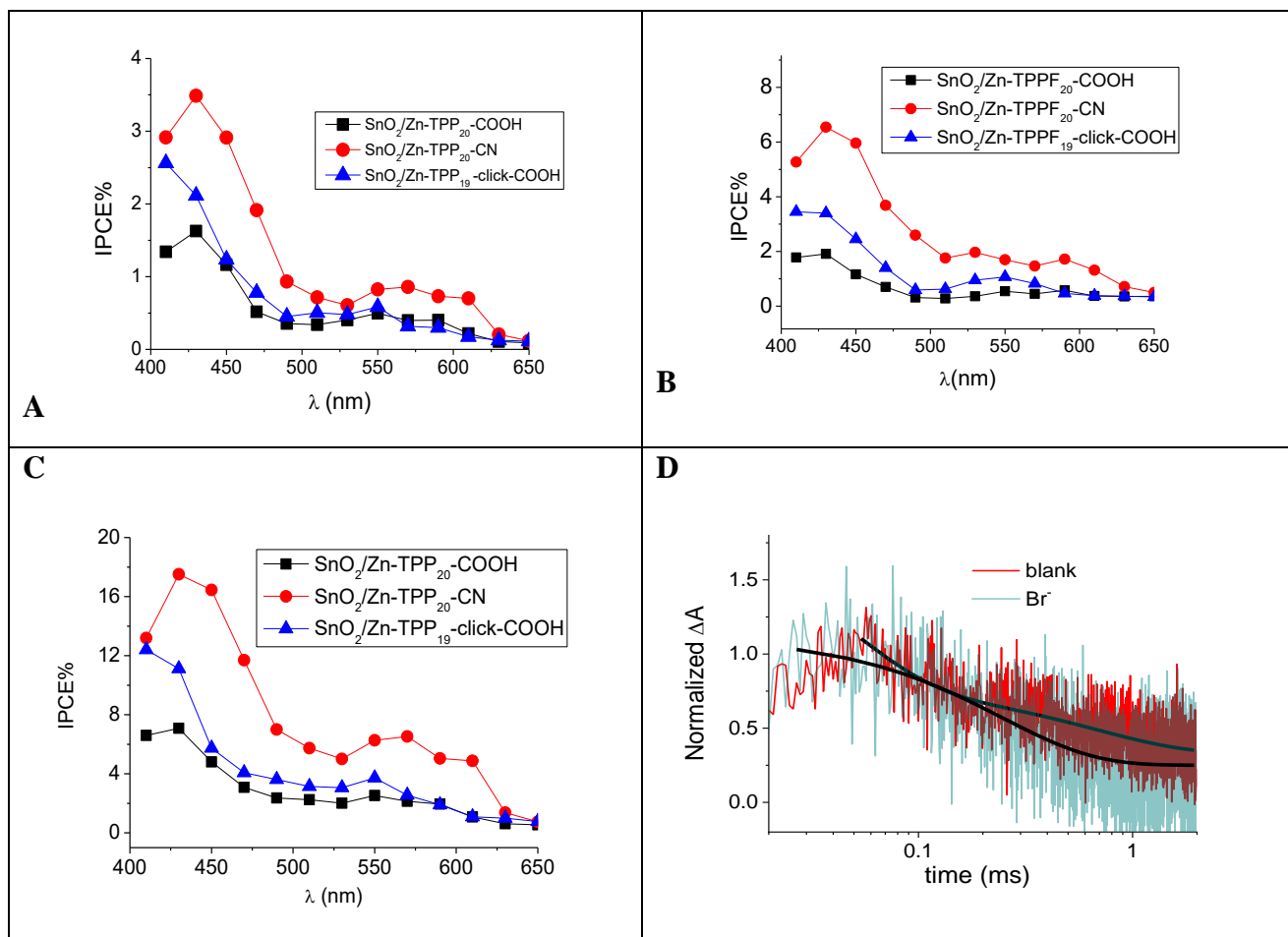
Figure 7. Photoaction spectra taken on SnO_2/TiO_2 sensitized substrate at 0.7 V : $SnO_2/ZnTPPF_{20}$-COOH, $SnO_2/ZnTPPF_{20}$-CN, $SnO_2/ZnTPPF_{19}$-click-COOH in: A) HBr 0.1M; B) HBr 0.1M, NaBr 0.3M; C) 0.1M ascorbic acid. D) 700 nm recovery of $ZnTPPF_{20}$-CN^+ loaded on SnO_2/TiO_2 in 0.1M $HClO_4$ (blank) and 0.3M NaBr, 0.1M HBr biased at 0.7 V vs Pt. Oscilloscope input impedance 10 kΩ.

Coupling to Water splitting redox catalyst

The proof of hole transfer from the porphyrin dyes immobilized on the TiO_2/SnO_2 photoanodes to a water oxidation catalyst, capable to oxidize water to di-oxygen under acidic conditions, was searched by co-adsorbing a binuclear iridium catalyst acting as the water oxidation catalyst, whose properties were previously reported on modified ITO.[35]

The successful adsorption of the binuclear Ir complex (Figure 8, IrWOC) on the SnO_2/TiO_2 $ZnTPPF_{20}$-CN photoanode, after two hours soaking, was testified by the appearance of a catalytic wave having onset at ca. 1.1 V vs SCE (Figure S45). Soaking of the dyed thin films in the catalyst solution was optimized by considering the long term response of the photoanode under constant potential chronoamperometry (Figure S46). The best initial performances were achieved after soaking for 1 hour, but the long term response was slightly better with the electrode subjected to 2

24

hour immersion in the catalyst solution, which was then adopted for all the subsequent experiments. Under these last conditions the ICP showed that the loading of ZnTPPF$_{20}$-CN was $(1.7\pm0.4) \times 10^{-8}$ Mol/cm^2 while Ir was $(2.5 \pm1.2)\ 10^{-9}$ Mol/cm^2. Leaching of ca. 30% of the initial Ir concentration however usually occurred during 1 hour photoelectrolysis under conventional open configuration cell (i.e. no thin layer cell).

Consistent with electron transfer from the co-adsorbed catalyst to Zn-TPPF$_{20}$-CN$^+$, the 700 nm absorption of the latter, undergoes a shortening, particularly evident from Figure 8 between 1 and 4 ms, resulting in a decreased τ_{av} from 3.26 to 2.15 ms (cyan line) when the catalyst is present. Irrespective of the presence of the water oxidation catalyst, the recovery of Zn-TPPF$_{20}$-CN$^+$ is incomplete on a time scale of 5 ms, and after 4 ms both the green and blue traces seem to evolve with a similar kinetics, probably indicating that only a fraction of Zn-TPPF$_{20}$-CN$^+$ has a sufficient coupling with the redox catalyst on the surface to give rise to electron transfer. Nevertheless, chronoamperometry of the SnO$_2$/TiO$_2$/ZnTPPF$_{20}$-CN/IrWOC in a thin layer cell under visible illumination ($\lambda> 450$ nm) demonstrate that the SnO$_2$/TiO$_2$/ZnTPPF$_{20}$-CN/IrWOC is able to split water with a high faradaic yield.

The photoanodic current generated by SnO$_2$/ZnTPPF$_{20}$-CN/IrWOC, where a bare FTO electrode biased at -0.6 V vs SCE under bipotentiostatic control serves as the oxygen collector (Scheme S1), was found to increase during the first 600 s, after which a constant value of ca. 0.1 mA/cm^2 was maintained (Figure 9B). The trend followed by the photoanodic current was mirrored by the cathodic current associated to oxygen reduction occurring at the counter electrode. At present we do not have a fully satisfying explanation to the observed evidence. Possibly, during the first minutes of operation, the Ir complex is converted to an IrO$_x$ species, more active in oxygen evolution. Previous studies however remarked an excellent stability of IrWOC with respect to oxidative degradation.[35] A better explanation could be the achievement of a steady state condition for the electrode under polarization and under illumination, related to desorption of part of the weakest adsorbed catalyst, which may both compete in light absorption with the porphyrin and cause excessive recombination.

Nonetheless, after attaining the steady state, the photocurrent was stable for thousand seconds even at a lower bias (0.3V vs SCE, Figure 9D), and was unambiguously associated to oxygen evolution, ceasing quickly in the absence of illumination. The calculated Faradaic yield, obtained from the integrated chronoamperograms according to the Faraday law, is independent from the applied bias and turns out to be larger than 95% in the presence of Ir-WOC compared to less than 10% when the catalyst is absent (Figure 9C and Figure S47).
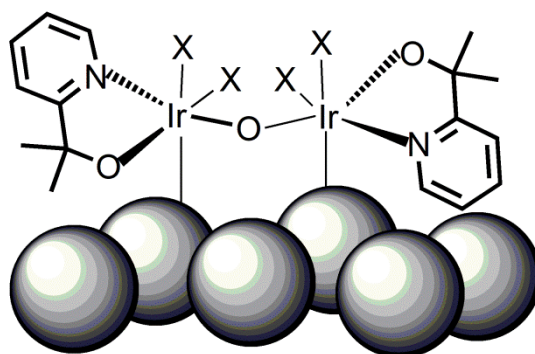
Figure 8. Schematic structure of the Binuclear Iridium(IV) (IrWOC) complex obtained following oxidation of the Ir^{III} monomer with $NaIO_4$. The complex is shown to interact with a mesoporous metal oxide. Recent findings suggest a single μ-oxo bridge between the two iridium atoms of the dimeric Ir-WOC.[36,37,38]
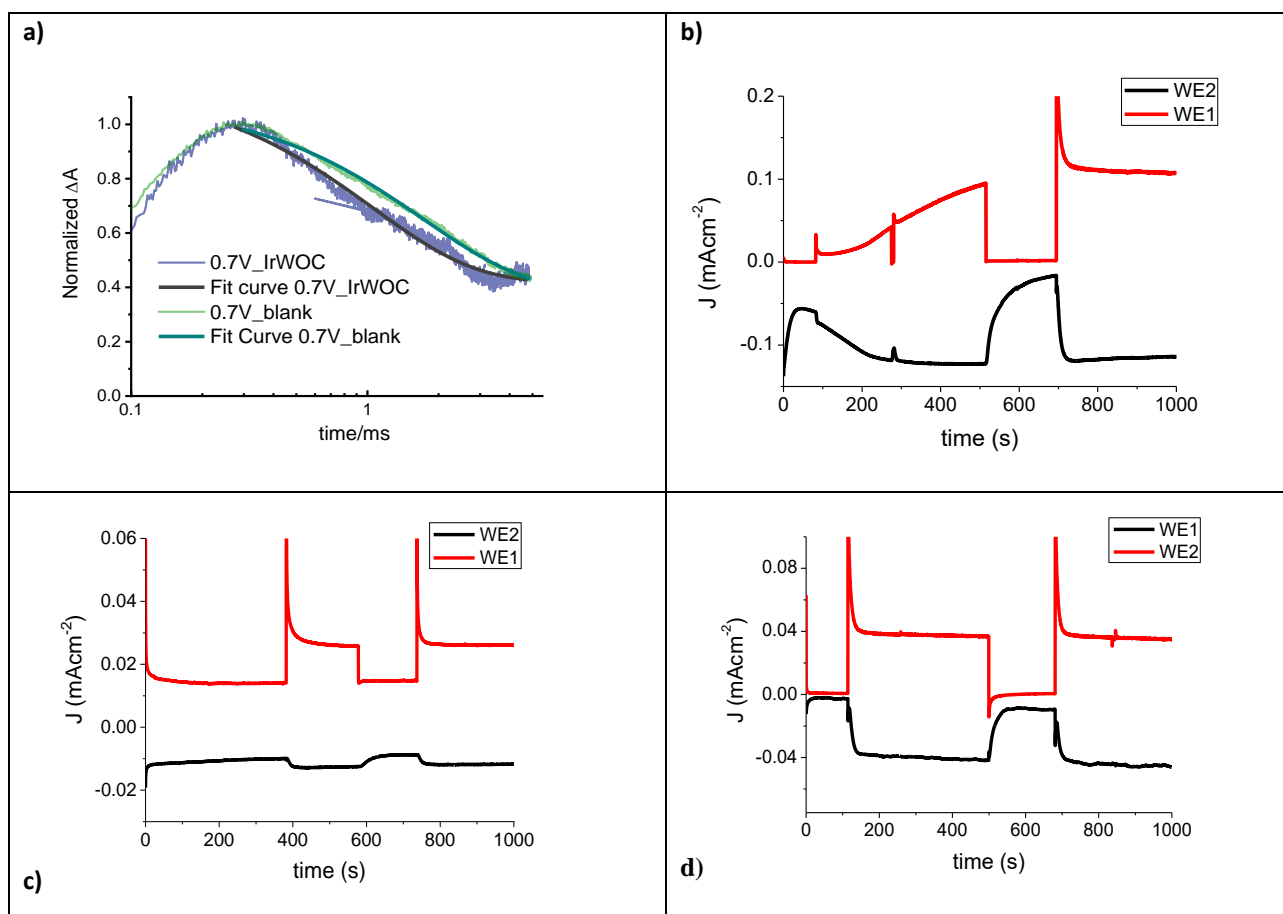

Figure 9 a) Recovery of ZnTPPF20-CN$^+$ in the absence (blank, green line) and in the presence of IrWOC (blue line) monitored at 700 nm. Oscilloscope impedance 1MΩ; (b)-(d) Photocurrent delivered by the photoanode (WE1) (red) associated to oxygen reduction (black) at the collector electrode (WE2) held at constant -0.6 V vs SCE. (b) $SnO_2/TiO_2/ZnTPPF_{20}$-CN/IrWOC at 0.7 V vs SCE; (c) $SnO_2/TiO_2/ZnTPPF_{20}$-CN at 0.7V vs SCE; (d) $SnO_2/TiO_2/ZnTPPF_{20}$-CN/IrWOC at 0. 3 V vs SCE; 0.1 M $HClO_4$, AM 1.5 G, with 450 nm cut off filter.

It can also be observed that the performances during generation/collection experiments in a thin layer cell are higher by at least ca. 30% and also more stable with respect to those found with the photoanode under open configuration (i.e. in a regular three electrodes cell, Figure S46), and that was attributed to the continuous removal of photogenerated oxygen by the collector electrode, oxygen that can otherwise locally accumulate at the surface of the photoanode whereupon is generated and act as an electron scavenger, reducing the photoanodic output of the cell.

Conclusions

A series of perfluorinated Zn^{II} porphyrins with different acceptor/linker groups was evaluated as n-type dyes for photoelectrosynthetic cells. The perfluorinated design was successful in creating an electron-poor porphyrin core, allowing to obtain a sufficiently positive ground state oxidation potential to trigger energetically demanding redox reactions for solar energy conversion and storage. The dye series was used to sensitize TiO_2 and SnO_2 substrates which displayed satisfactory adsorption stability in acidic water, thanks to the hydrophobic properties of these dyes. Nevertheless, the perfluorinated design increased the reorganization energy and decreased the coupling of the excited state with the semiconductor, resulting in relatively low injection yields, which were found, in the best case, of the order of 12% with SnO_2 based electrodes. Better results, with yields of the order of 15-18 % were found in the presence of AA, thanks to the reductive quenching of the triplet excited state and the injection from the reduced state of the dye. Consistent with the calculations, the best results, were found for $ZnTPPF_{20}$-CN bearing the cyanoacrylic group as the strongest electron withdrawing group, leading to the best coupling for injection. $ZnTPPF_{20}$-CN was thus the best performer in the splitting of HBr (APCE % = 6/7 %) and, when coupled to a suitable catalyst, of water, where a stable photoanode operation in acidic conditions was observed, exploiting visible radiation up to 650 nm with nearly quantitative faradaic yield. Thus the perfluorinated porphyrins equipped with cyanoacrylic terminal group at the β-position, should be considered for further development intended to improve the charge transfer character. For example, the insertion of strong electron acceptors in the linker arm might increase the electronic coupling for charge injection, while the use of CF_3 substituted phenyl groups might further enhance dye stability. At the same time, by exploiting the information gained by this study, we are now trying to fabricate molecular dyads integrating both porphyrin dyes and catalytic complexes, where reductive quenching of the porphyrin excited state will simultaneously increase both the injection quantum yield and activate the catalyst for oxygen evolution.

Acknowledgements

References

(1)   Faunce, T.; Styring, S.; Wasielewski, M. R.; Brudvig, G. W.; Rutherford, A. W.; Messinger, J.; Lee, A. F.; Hill, C. L.; Fontecave, M.; Macfarlane, D. R.; Hankamer, B.; Nocera, D. G.; Tiede, D. M.; Dau, H.; Hillier, W.; Wang, L.; Amal, R. Artificial Photosynthesis as a Frontier Technology for Energy Sustainability. Energy Environ. Sci. **2013**, *6*, 1074–1076. https://doi.org/10.1039/c3ee40534f.

(2)   Brennaman, M. K.; Dillon, R. J.; Alibabaei, L.; Gish, M. K.; Dares, C. J.; Ashford, D. L.; House, R. L.; Meyer, G. J.; Papanikolas, J. M.; Meyer, T. J. Finding the Way to Solar Fuels with Dye-Sensitized Photoelectrosynthesis Cells. *J. Am. Chem. Soc.* **2016**, *138* (40), 13085–13102. https://doi.org/10.1021/jacs.6b06466.

(3)   Mei, B.; Mul, G.; Seger, B. Beyond Water Splitting: Efficiencies of Photo-Electrochemical Devices Producing Hydrogen and Valuable Oxidation Products. *Adv. Sustain. Syst.* **2017**, *1*, 1600035-1600040. https://doi.org/10.1002/adsu.201600035.

(4)   Brady, M. D.; Troian-gautier, L.; Sampaio, R. N.; Motley, T. C.; Meyer, G. J.; Carolina, N.; Hall, M.; Hill, C.; Carolina, N. Optimization of Photocatalyst Excited- and Ground-State Reduction Potentials for Dye-Sensitized HBr Splitting. *ACS Appl. Mater. Interfaces* **2018**, *10*, 31312–31323. https://doi.org/10.1021/acsami.8b09134.

(5)   Brady, M. D.; Sampaio, R. N.; Wang, D.; Meyer, T. J.; Meyer, G. J. Dye-Sensitized Hydrobromic Acid Splitting for Hydrogen Solar Fuel Production. *J. Am. Chem. Soc.* **2017**, *139* (44), 15612–15615. https://doi.org/10.1021/jacs.7b09367.

(6)   Mussini, P. R.; Orbelli Biroli, A.; Tessore, F.; Pizzotti, M.; Biaggi, C.; Di Carlo, G.; Lobello, M. G. M. G.; De Angelis, F. Modulating the Electronic Properties of Asymmetric Push-Pull

and Symmetric Zn(II)-Diarylporphyrinates with Para Substituted Phenylethynyl Moieties in 5,15 Meso Positions: A Combined Electrochemical and Spectroscopic Investigation. *Electrochim. Acta* **2012**, *85*, 509–523. https://doi.org/10.1016/j.electacta.2012.08.039.

(7) Yella, A.; Lee, H. W.; Tsao, H. N.; Yi, C.; Chandiran, A. K.; Nazeeruddin, M. K.; Diau, E. W. G.; Yeh, C. Y.; Zakeeruddin, S. M.; Grätzel, M. Porphyrin-Sensitized Solar Cells with Cobalt(II/III)-Based Redox Electrolyte Exceed 12 Percent Efficiency. *Science* **2011**, *334*, 629–634. https://doi.org/10.1126/science.1209688.

(8) Wang, Y.; Chen, B.; Wu, W.; Li, X.; Zhu, W.; Tian, H.; Xie, Y. Efficient Solar Cells Sensitized by Porphyrins with an Extended Conjugation Framework and a Carbazole Donor : From Molecular Design to Cosensitization. *Angew. Chem. Int. Ed.* **2014**, *53*, 10779–10783. https://doi.org/10.1002/anie.201406190.

(9) Xie, Y.; Tang, Y.; Wu, W.; Wang, Y.; Liu, J.; Li, X.; Tian, H.; Zhu, W. H. Porphyrin Cosensitization for a Photovoltaic Efficiency of 11.5%: A Record for Non-Ruthenium Solar Cells Based on Iodine Electrolyte. *J. Am. Chem. Soc.* **2015**, *137* (44), 14055–14058. https://doi.org/10.1021/jacs.5b09665.

(10) Moore, G. F.; Blakemore, J. D.; Milot, R. L.; Hull, J. F.; Song, H. E.; Cai, L.; Schmuttenmaer, C. A.; Crabtree, R. H.; Brudvig, G. W. A Visible Light Water-Splitting Cell with a Photoanode Formed by Codeposition of a High-Potential Porphyrin and an Iridium Water-Oxidation Catalyst. *Energy Environ. Sci.* **2011**, *4* (7), 2389–2392. https://doi.org/10.1039/c1ee01037a.

(11) Materna, K. L.; Jiang, J.; Regan, K. P.; Schmuttenmaer, C. A.; Crabtree, R. H.; Brudvig, G. W. Optimization of Photoanodes for Photocatalytic Water Oxidation by Combining a Heterogenized Iridium Water-Oxidation Catalyst with a High-Potential Porphyrin Photosensitizer. *ChemSusChem* **2017**, *10* (22), 4526–4534. https://doi.org/10.1002/cssc.201701693.

(12) Nayak, A.; Knauf, R. R.; Hanson, K.; Alibabaei, L.; Concepcion, J. J.; Ashford, D. L.; Dempsey, J. L.; Meyer, T. J. Synthesis and Photophysical Characterization of Porphyrin and Porphyrin-Ru(II) Polypyridyne Chromophore-Catalyst Assemblies on Mesoporous Metal Oxides. *Chem. Sci.* **2014**, *5*, 3115–3119. https://doi.org/10.1039/c4sc00875h.

(13) Milot, R. L.; Schmuttenmaer, C. A. Electron Injection Dynamics in High-Potential Porphyrin Photoanodes. *Acc. Chem. Res.* **2015**, *48* (5), 1423–1431. https://doi.org/10.1021/ar500363q.

(14) Lim, G. N.; Hedstro, S.; Jung, K. A.; Smith, P. A. D.; Batista, V. S.; D'Souza, F.; Van Der Est, A.; Poddutoori, P. K. Interfacial Electron Transfer Followed by Photooxidation In *N,N*-Bis(*p*-anisole)aminopyridine-Aluminum(III) Porphyrin-Titanium(IV) Oxide Self-Assembled Photoanodes. *J.Phys. Chem. C* **2017**, *121*, 14484-14497. https://doi.org/10.1021/acs.jpcc.7b04197.

(15) Lee, S. H.; Regan, K. P.; Hedström, S.; Matula, A. J.; Chaudhuri, S.; Crabtree, R. H.; Batista, V. S.; Schmuttenmaer, C. A.; Brudvig, G. W. Linker Length-Dependent Electron-Injection Dynamics of Trimesitylporphyrins on SnO$_2$ Films. *J. Phys. Chem. C* **2017**, *121* (41), 22690–22699. https://doi.org/10.1021/acs.jpcc.7b07855.

(16) Lindsey, J. S.; Schreiman, I. C.; Hsu, H. C.; Kearney, P. C.; Marguerettaz, A. M. Rothemund and Adler-Longo Reactions Revisisted: Synthesis of Tetraphenylporphyrins under Equilibrium Conditions. *J. Org. Chem.* **1987**, *52*, 827–836.

(17) Di Carlo, G.; Orbelli Biroli, A.; Pizzotti, M.; Tessore, F.; Trifiletti, V.; Ruffo, R.; Abbotto, A.; Amat, A.; De Angelis, F.; Mussini, P. R. Tetraaryl Zn^{II} Porphyrinates Substituted at β-Pyrrolic Positions as Sensitizers in Dye-Sensitized Solar Cells: A Comparison with Meso-Disubstituted Push-Pull Zn^{II} Porphyrinates. *Chem. Eur. J.* **2013**, *19* (32), 10723–10740. https://doi.org/10.1002/chem.201300219.

(18) Golf, H. R. A.; Reissig, H. U.; Wiehe, A. Regioselective Nucleophilic Aromatic Substitution Reaction of Meso-Pentafluorophenyl-Substituted Porphyrinoids with Alcohols. *Eur. J. Org. Chem.* **2015**, *2015* (7), 1548–1568. https://doi.org/10.1002/ejoc.201403503.

(19) Kolb, H. C.; Finn, M. G.; Sharpless, K. B. Click Chemistry: Diverse Chemical Function from a Few Good Reactions. *Angew. Chem. Int. Ed.* **2001**, *40,*, 2004-2021. https://doi.org/10.1002/chin.200135279.

(20) Colombo, A.; Di Carlo, G.; Dragonetti, C.; Magni, M.; Orbelli Biroli, A.; Pizzotti, M.; Roberto, D.; Tessore, F.; Benazzi, E.; Bignozzi, C. A.; Casarin, L.; Caramori, S. Coupling of Zinc Porphyrin Dyes and Copper Electrolytes: A Springboard for Novel Sustainable Dye-Sensitized Solar Cells. *Inorg. Chem.* **2017**, *56* (22), 14189-141976. https://doi.org/10.1021/acs.inorgchem.7b02323.

(21) Gritzner, G.; Kůta, J. Recommendations on Reporting Electrode Potentials in Nonaqueous Solvents: IUPC Commission on Electrochemistry. *Electrochim. Acta* **1984**, *29* (6), 869–873. https://doi.org/10.1016/0013-4686(84)80027-4.

(22) Carlo, G. Di; Caramori, S.; Tri, V.; Giannuzzi, R.; Marco, L. De; Pizzotti, M.; Orbelli Biroli, A.; Tessore, F.; Argazzi, R.; Bignozzi, C. A. Influence of Porphyrinic Structure on Electron Transfer Processes at the Electrolyte/Dye/TiO$_2$ Interface in PSSCs: A Comparison between Meso Push−Pull and β‑Pyrrolic Architectures. *ACS Appl. Mater. Interfaces* **2014**, *6*, 15841−15852.

(23) Kim, D.; Holten, D.; Gouterman, M. Evidence From Picosecond Transient Absorption and Kinetic Studies of Charge-Transfer States in Copper(II) Porphyrins. *J. Am. Chem. Soc.* **1984**, *106* (10), 2793–2798. https://doi.org/10.1021/ja00322a012.

(24) Young, K. J.; Martini, L. A.; Milot, R. L.; Snoeberger III, R. C.; Batista, V. S.; Schmuttenmaer, C. A.; Crabtree, R. H.; Brudvig, G. W. Light-Driven Water Oxidation for Solar Fuels. *Coord. Chem. Rev.* **2012**, *256* (1), 2503–2520. https://doi.org/10.1016/j.ccr.2012.03.031.Light-driven.

(25) Di Carlo, G.; Caramori, S.; Casarin, L.; Orbelli Biroli, A.; Tessore, F.; Argazzi, R.; Oriana, A.; Cerullo, G.; Bignozzi, C. A. C. A.; Pizzotti, M. Charge Transfer Dynamics in β- And Meso-Substituted Dithienylethylene Porphyrins. *J. Phys. Chem. C* **2017**, *121* (34), 18385–18400. https://doi.org/10.1021/acs.jpcc.7b05823.

(26) Enright, B.; Redmond, G.; Fitzmaurice, D. Spectroscopic Determination of Flatband Potentials for Polycrystalline TiO$_2$ Electrodes in Mixed Solvent Systems. *J. Phys. Chem.* **1994**, *98* (24), 6195–6200. https://doi.org/10.1021/j100075a023.

(27) Wilkinson, G.; Gillard, R. D.; McCleverty, J. A. *Comprehensive Coordination Chemistry : The Synthesis, Reactions, Properties & Applications of Coordination Compounds*; Pergamon Press, 1987.

(28) Wasielewski, M. R.; Niemczyk, M. P.; Svec, W. A.; Pewitt, E. B. Dependence of Rate Constants for Photoinduced Charge Separation and Dark Charge Recombination on the Free Energy of Reaction in Restricted-Distance Porphyrin-Quinone Molecules. *J. Am. Chem. Soc.* **1985**, *107* (4), 1080–1082. https://doi.org/10.1021/ja00290a066.

(29) Sun, H.; Smirnov, V. V.; DiMagno, S. G. Slow Electron Transfer Rates for Fluorinated Cobalt Porphyrins: Electronic and Conformational Factors Modulating Metalloporphyrin ET. *Inorg. Chem.* **2003**, *42* (19), 6032–6040. https://doi.org/10.1021/ic034705o.

(30) Bergeron, B. V.; Marton, A.; Oskam, G.; Meyer, G. J. Dye-Sensitized SnO$_2$ Electrodes with

Iodide and Pseudohalide Redox Mediators. *J. Phys. Chem. B* **2005**, *109* (2), 937–943. https://doi.org/10.1021/jp0461347.

(31) Alibabaei, L.; Brennaman, M. K.; Norris, M. R.; Kalanyan, B.; Song, W.; Losego, M. D.; Concepcion, J. J.; Binstead, R. A.; Parsons, G. N.; Meyer, T. J. Solar Water Splitting in a Molecular Photoelectrochemical Cell. *Proc. Natl. Acad. Sci.* **2013**, *110* (50), 20008–20013. https://doi.org/10.1073/pnas.1319628110.

(32) Alibabaei, L.; Sherman, B. D.; Norris, M. R.; Brennaman, M. K.; Meyer, T. J. Visible Photoelectrochemical Water Splitting into H_2 and O_2 in a Dye-Sensitized Photoelectrosynthesis Cell . *Proc. Natl. Acad. Sci.* **2015**, *112* (19), 5899–5902. https://doi.org/10.1073/pnas.1506111112.

(33) Sheridan, M. V.; Wang, Y.; Wang, D.; Troian-Gautier, L.; Dares, C. J.; Sherman, B. D.; Meyer, T. J. Light-Driven Water Splitting Mediated by Photogenerated Bromine. *Angew. Chem. Int. Ed.* **2018**, *57* (13), 3449–3453. https://doi.org/10.1002/anie.201708879.

(34) Ronconi, F.; Santoni, M. P.; Nastasi, F.; Bruno, G.; Argazzi, R.; Berardi, S.; Caramori, S.; Bignozzi, C. A.; Campagna, S. Charge Injection into Nanostructured TiO_2 Electrodes from the Photogenerated Reduced Form of a New Ru(II) Polypyridine Compound: The "Anti-Biomimetic" Mechanism at Work. *Dalton Trans.* **2016**, *45* (36), 14109–14123. https://doi.org/10.1039/c6dt01970f.

(35) Graeupner, J.; Hintermair, U.; Huang, D. L.; Thomsen, J. M.; Takase, M.; Campos, J.; Hashmi, S. M.; Elimelech, M.; Brudvig, G. W.; Crabtree, R. H. Probing the Viability of Oxo-Coupling Pathways in Iridium-Catalyzed Oxygen Evolution. *Organometallics* **2013**, *32* (19), 5384–5390. https://doi.org/10.1021/om400658a.

(36) Sharninghausen, L. S.; Sinha, S. B.; Shopov, D. Y.; Choi, B.; Mercado, B. Q.; Roy, X.; Balcells, D.; Brudvig, G. W.; Crabtree, R. H. High Oxidation State Iridium Mono-μ-Oxo Dimers Related to Water Oxidation Catalysis. *J. Am. Chem. Soc.* **2016**, *138* (49), 15917–15926. https://doi.org/10.1021/jacs.6b07716.

(37) Sinha, S. B.; Shopov, D. Y.; Sharninghausen, L. S.; Stein, C. J.; Mercado, B. Q.; Balcells, D.; Pedersen, T. B.; Reiher, M.; Brudvig, G. W.; Crabtree, R. H. Redox Activity of Oxo-Bridged Iridium Dimers in an N,O-Donor Environment: Characterization of Remarkably Stable Ir(IV,V) Complexes. *J. Am. Chem. Soc.* **2017**, *139* (28), 9672–9683. https://doi.org/10.1021/jacs.7b04874.

(38) Michaelos, T. K.; Shopov, D. Y.; Sinha, S. B.; Sharninghausen, L. S.; Fisher, K. J.; Lant, H. M. C.; Crabtree, R. H.; Brudvig, G. W. A Pyridine Alkoxide Chelate Ligand That Promotes Both Unusually High Oxidation States and Water-Oxidation Catalysis. *Acc. Chem. Res.* **2017**, *50* (4), 952–959. https://doi.org/10.1021/acs.accounts.6b00652.

Graphic for manuscript
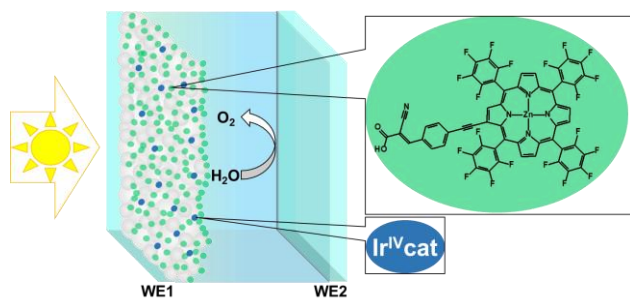
Supporting Information

The SI contain: i) the syntheses and characterization of the dyes; ii) the preparation of the photonades; iii) the computational results; iv) the spectroscopic and electrochemical characterization of the sensitized photoanodes; v) the transient absorption spectra; vi) the current-voltage curves and the photoaction spectra in the presence of hole scavengers; vii) the cyclic voltammetry and chronoamperometry curves after coupling to water splitting redox catalyst.